IOP Publishing J. Phys. Energy 3 (2021) 024003 https://doi.org/10.1088/2515-7655/abd297

Journal of Physics: Energy

OPEN ACCESS

RECEIVED
29 September 2020

REVISED
16 November 2020

ACCEPTED FOR PUBLICATION
10 December 2020

PUBLISHED
28 January 2021

PAPER

Colossal grain growth in Cd(Se,Te) thin films and their subsequent use in CdTe epitaxy by close-spaced sublimation

David S Albin[1], **Mahisha Amarasinghe**[1,2], **Matthew O Reese**[1], **John Moseley**[1], **Helio Moutinho**[1] and **Wyatt K Metzger**[1]

[1] National Renewable Energy Laboratory, Golden, CO 80401, United States of America
[2] Department of Physics, University of Illinois at Chicago, Chicago, IL 60607, United States of America

E-mail: david.albin@nrel.gov

Keywords: CdTe, polycrystalline thin films, nucleation and growth, epitaxy, explosive recrystallization, solar cell

Abstract

Many technologies deposit thin films on inexpensive substrates, resulting in small grains due to classic nucleation and grain growth theory. For example, state-of-the-art solar cells are made by depositing CdSeTe and CdTe layers on inexpensive glass coated with nanocrystalline transparent conducting oxides (TCOs), like SnO_2. Characteristically, the grain size of these films is on the order of the film thickness, i.e. a few microns. CdTe small-grain films have poor electro-optical properties and require $CdCl_2$ passivation which fails to fully passivate grain boundaries, causes carrier compensation, and prevents implementing other II–VI alloys and materials to improve performance. Here, we present a method to increase grain size to 1 mm in $CdSe_xTe_{1-x}$ thin films deposited on glass/TCO substrates without $CdCl_2$ treatment. The colossal grain growth is driven by mechanisms distinct from classic nucleation, grain growth, and Ostwald ripening and only occurs at low selenium content ($x \sim 0.1$). We also demonstrate how these films can serve as templates for subsequent large-grain epitaxy of other compositions like CdTe, again without exposure to $CdCl_2$. The results open new paths for thin film solar cell technology, and thin film devices in general.

1. Introduction

1.1. CdTe solar cell technology

Polycrystalline (pX) thin films for solar cell applications can be deposited very quickly using high throughput deposition techniques and inexpensive substrates such as glass and metal foils. Consequently, it offers a different paradigm than traditional melt-solidification of single-crystal Si wafers over the course of multiple steps and days of growth, or epitaxial growth at the rate of $\sim$1 μm h^{-1} on expensive single crystals. Thus, the leading U.S. solar cell photovoltaic (PV) technology in cost/watt is based on pX-CdTe thin films, which have produced state-of-the-art solar device performance with costs less than conventional fuels [1].

Typically, fast film deposition on glass, metal foils, and nanocrystalline layers like TCO/glass produce small grains. Consequently, recombination at resulting grain boundaries (GBs) can limit the performance of solar cells using these substrates [2]. Fortunately, the ubiquitous technique of annealing CdTe films and devices in $CdCl_2$ to passivate GBs has overcome some of the inherent problems associated with smaller grains, increasing minority carrier lifetime from tens of ps to tens of ns [3, 4]. With a passivated absorber layer, CdTe solar cell performance has recently improved by using more transparent buffer layers like (Mg,Zn)O [5–8] and bandgap engineering at the junction using Se, e.g. CdSe or Cd(Se,Te) alloys [9–14]. A further advantage of Se is that when combined with $CdCl_2$, GB passivation is improved relative to $CdCl_2$ use alone [12, 15, 16].

In addition, a technology shift towards using CdTe films extrinsically doped with Group V (GrV) elements is also expected [17]. These dopants provide a path to increase built-in potential, and thus CdTe solar cell performance [18]. First, it is a viable way to supplant Cu doping which is highly compensated by Cl, historically limiting hole densities to about 10^{14} cm^{-3} [19, 20]. For example, GrV dopants have increased the hole density in pX-CdTe and CdSeTe in excess of 10^{16} cm^{-3} [21, 22]. Equally important, high carrier

densities resulting from the use of GrV dopants are more stable relative to Cu and may improve CdTe solar cell reliability [17, 23]. While GrV dopants have improved hole density, the activation ratio remains low relative to single crystal and epitaxial materials where Cl is not used [24, 25]. This compensation can cause potential fluctuations that limit open-circuit voltage (V_{oc}), and it is possible that eliminating Cl could help increase the activation ratio [2, 26]. With increased hole density and consequently smaller depletion width, added importance will be placed on carrier collection or recombination outside the space-charge region. Many of the convoluting effects associated with carrier density and recombination in pX-CdTe have been studied by Kanevce *et al* [27]. In addition to the critical need to reduce junction recombination, the benefits of higher hole density require a reduction of the 'aggregate' recombination in the bulk (intragrain and GB). In the specific case of reduced junction recombination and increasing intragrain lifetimes, modeling shows (see for example figure 5 in [27]) that increasing the grain size will reduce the effects of GB recombination on aggregate bulk lifetime. By increasing bulk lifetime to 100 ns and beyond, back surface fields, passivation, and reflectors can more effectively increase performance, as well as enable bifacial [28, 29] and interdigitated back contact solar technology [30], providing paths to 28% cell efficiency. For this technology to continue to advance, new methods to reduce recombination and approach single crystal quality—while maintaining low costs—are justified.

1.2. Film growth

Numerous techniques exist for depositing polycrystalline thin films. Many, like vapor transport deposition (VTD) and close-spaced sublimation (CSS), are physical deposition processes where source material is vaporized and transported to cooler substrates in low to high vacuum conditions. Other than how adatoms interact, reactive chemistries, like those in chemical vapor deposition, are not usually considered in these physical methods. The classic homogenous (i.e. substrate-free) vapor-to-solid nucleation model assuming spherical nuclei thus involves minimizing the Gibbs free energy,

$$\Delta G = 4\pi r^2\gamma + \frac{4}{3}\pi r^3 \Delta G_v \tag{1}$$

where γ and r are the surface energy and radius of the condensed phase respectively, and ΔG_v is the volume free energy change associated with vapor-to-solid condensation. Since solids are denser than vapors, ΔG_v is always negative and equation (1) represents a balance between increasing area and decreasing volume. With increasing radius, ΔG initially increases but eventually, the r^3 term dominates and ΔG becomes negative. The net result is that there is a maximum value for ΔG, labeled ΔG^*, corresponding to a critical radius, r^*. Nuclei with $r < r^3$ are unstable and dissociate, while nuclei with $r > r^*$ continue to grow to reduce total system energy.

The morphology of deposited films is affected by both ΔG^* and r^*, as well as subsequent grain growth and coalescence. When growth conditions favor smaller barriers (ΔG^*) and nuclei (r^*), many nucleation sites develop resulting in smaller-grained films. In contrast, higher energy barriers with larger critical radii reduce nucleation site density resulting in larger-grain morphologies and even epitaxy.

For the isothermal condensation of an ideal gas, ΔG_v is related to the ratios of the saturated vapor pressure, P_s and the equilibrium partial pressure of the solid, P_o [31]:

$$\Delta G_v \propto -\ln\left(P_s/P_o\right) \tag{2}$$

For equation (1) to be negative, a necessary requirement for nucleation is that $P_s > P_o$, i.e. the vapor is supersaturated relative to condensed phase.

$\Delta G^*$and r^* can be solved directly from equation (1) by setting the derivative with respect to r equal to zero, from which the following relationships are derived:

$$\Delta G^*_{homo} = \frac{16\pi\gamma^3}{3(\Delta G_v)^2} \tag{3a}$$

$$r^*_{homo} = \frac{-2\gamma}{\Delta G_v} \tag{3b}$$

Again, homogeneous nucleation is implied. For the specific case of heterogeneous nucleation on a substrate, equation (3*a*) is modified to include the interaction of surface energy terms for the film-substrate (γ_{fs}), substrate-vapor (γ_{sv}), and film-vapor (γ_{fv}) interfaces through a film/substrate contact angle, θ. In doing so, the heterogeneous nucleation barrier, ΔG^*_{het} is represented as [32]:

$$\Delta G^*_{het} = \Delta G^*_{homo} \cdot f(\theta) \text{ where } f(\theta) = \left(\frac{2 - 3\cos\theta + \cos^3\theta}{4}\right) \tag{4}$$

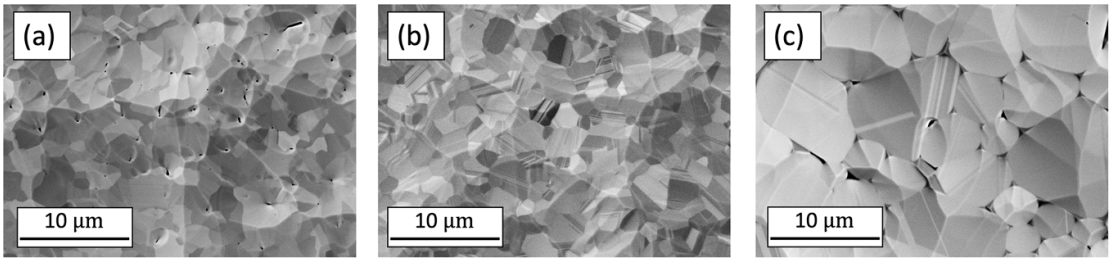

Figure 1. As-deposited (no $CdCl_2$) CdTe film (a); $CdCl_2$ treated at 440 °C (b); $CdCl_2$ treated at 490 °C (c). SEM imaged at 0° tilt with original image taken at 3.5 kX magnification.

Here, r^* remains unchanged from equation (3*b*), and γ is replaced by γ_{fv}. The function $f(\theta)$ varies from 0 to 1 as θ varies from the case of complete wetting (0°) to complete de-wetting (180°), at which point the nuclei takes the shape of a sphere and represents homogeneous nucleation. It is also clear from equation (4) that heterogeneous nucleation barriers are smaller than those for homogeneous nucleation.

Once stable nuclei form and grow into islands or 'grains' they coalesce creating GBs where the as-deposited, morphology is again largely determined by nucleation conditions. In vapor deposited CdTe and CdSeTe thin films, the high nucleation site density presented by small-grained pX-CdSe, (Mg,Zn)O, or SnO_2 substrates, combined with lower adatom surface mobility resulting from lower substrate temperatures to reduce re-evaporation (i.e. maximize condensation), result in as-deposited films with nm to μm size grains. Both equiaxed and columnar, fiber-like structures can result depending on substrate temperature and deposition rate. Because grain size (GS) is lognormally distributed, grain growth during deposition and subsequent thermal anneals occur as large grains consume smaller ones to reduce the surface energy represented by GBs. Grain growth rates are slow since GB mobility scales with self-diffusivities [31]. Once the average GS is comparable to the film thickness, normal grain growth slows and eventually stops. The resulting structure of as-grown thin films have a grain size-to-thickness (GS/t) ratio on the order of 1. Ratios on this order or less have been the norm for CdTe solar technology for decades across many different institutions.

In CdTe thin films, GS/$t > 1$ results from secondary grain growth when $CdCl_2$ is used as a fluxing agent since it forms a eutectic with CdTe at about 505 °C [33]. The growth mechanism is similar to Ostwald ripening where the eutectic facilitates the formation of a liquid phase that provides a means for atoms on small grains to dissolve into a liquid matrix where subsequent supersaturation leads to nucleation on larger grains. The result can be observed by the development of a bimodal distribution of grain sizes from an initially broader, smaller-sized distribution. The transition to secondary grain growth with $CdCl_2$ is shown in figure 1.

In this example, 5–7 μm thick CdTe films were evaporated on (Mg,Zn)O coated TEC12D (SnO_2-coated soda-lime glass made by Pilkington) substrates by CSS using source and substrate temperatures of 660 °C and 600 °C, respectively, in an oxygen containing ambient. Normal grain size in the as-deposited film (before $CdCl_2$) results in a GS/t ratio of ~1 as seen in figure 1(a). With a $CdCl_2$ anneal of 440 °C, grain growth is limited though some pore elimination and densification is apparent in figure 1(b). It should be noted that in cases where initial grain size is smaller (e.g. as when using lower substrate temperatures), growth can be significantly greater at this or even lower $CdCl_2$ anneal temperatures [34, 35]. As the $CdCl_2$ anneal temperature approaches the eutectic, Ostwald ripening dominates leading to significant grain growth as well as the development of a bimodal grain-size distribution (small and large grains) as seen in figure 1(c).

Unfortunately, a common drawback of relying upon Ostwald ripening for grain growth is the increased porosity at GB triple-points (figure 1(c)). This can increase front-to-back terminal shunting in PV devices and decrease adhesion, potentially leading to film delamination. Lower anneal temperatures of around 450 °C therefore represent a reasonable upper limit for $CdCl_2$ anneals where secondary growth is limited to only 5–10 microns. We remind the reader though, that the major reason for $CdCl_2$ is not grain growth per se, but rather to improve device performance by lowering GB and interface recombination in systemically small-grain pX thin-film morphologies. As was mentioned previously, carrier lifetimes in as-deposited films are on the order of tens of picoseconds. However, this high recombination does not appear to be related to intragranular defects. For example, intragranular lifetimes for CdTe were determined by measuring two-photon excitation time-resolved photoluminescence (2PE-TRPL) decays using very large grain and thick (both ~100 micron) CdTe films where excitation occurred within a single grain. An intragrain lifetime of 30 ns was measured without $CdCl_2$ anneals [36]. This raises the possibility that $CdCl_2$ anneals might not be required if for example, GB recombination, and thus aggregate recombination can be effectively reduced by using pX films with much larger grain sizes.

One way to economically realize larger grain pX-CdTe thin films is by depositing the CdTe on substrates (or templates) that themselves consist of larger-grained film morphologies using rapid deposition techniques like CSS or VTD. For example, the grain size of pX-CdTe thin films deposited using CSS was recently shown as being dependent primarily on the grain size of the substrate or template itself. Epitaxy resulting from CSS deposition was observed on both very large, molecular beam epitaxy (MBE) grown single-crystal CdTe templates as well as large-grained (~10 μm) pX-CdTe templates [37, 38]. Thus, if large grain size templates could be made cheaply, these could be used to cheaply manufacture very large-grained, CdTe solar cells.

In this paper, we demonstrate a new, colossal grain growth (CGG) method that results in 1 mm sized grains in uniformly thin, high crystalline Cd(Se,Te) films without $CdCl_2$ anneals. These films have GS/t ratios exceeding 100, which is orders of magnitude greater than anything previously observed or reported. In addition, we demonstrate the viable use of these large-grain films as 'templates' for epitaxially growing similarly large-grained CdTe films using CSS as a deposition technique. The resulting structure is very relevant to current state-of-the-art CdTe solar cells in which the CdTe is deposited on Se-containing thin films (e.g. CdSe or Cd(Se,Te) alloys).

2. Experimental methods

2.1. Film deposition

Vapor deposition techniques used to deposit pX-CdTe and Cd(Se,Te) films included conventional vacuum evaporation and CSS. Vacuum evaporation of $CdSe_{0.10}Te_{0.9}$ alloy source materials from 5 N Plus [39] used a Veeco evaporator with a base pressure of $\sim 10^{-6}$ Torr to deposit precursor films that were subsequently used as templates for CdTe epitaxy using both CSS and VTD. The evaporant source particle size was −60/+200 mesh. Typical source (T_{src}) and substrate (T_{sub}) temperatures were 660 °C–675 °C and 450 °C respectively, with an approximate source-to-substrate separation of 30 cm. Quartz wool minimized spitting from electrically heated alumina crucibles. Under these conditions, as-deposited pX films had very small grain sizes typically less than 100 nm. A slight loss of selenium was observed during evaporation based on comparing x-ray diffraction (XRD) measurements of the source powder relative to the deposited film. $CdSe_{0.10}Te_{0.9}$ alloy films used for subsequent CGG and epitaxy were typically between 1 and 6 microns in thickness.

The $CdSe_{0.10}Te_{0.9}$ was evaporated onto several substrate types. Most substrates consisted of 0.7 mm Corning 7059 glass (an alkali free, borosilicate glass) coated by 100 nm of alumina deposited by e-beam evaporation. Some films were also deposited on (Mg,Zn)O coated 7059 glass substrates where the (Mg,Zn)O represents a valid TCO growth surface for device fabrication.

$CdSe_{0.10}Te_{0.9}$ alloy films underwent thermal anneals to initiate the CGG process. Most anneals consisted of a CSS 'proximity' anneal where the small-grained alloy film/substrate was positioned 2 mm above a graphite plate film-side down over a well containing a $CdSe_{0.4}Te_{0.6}$ 5 N Plus anneal powder of similar mesh to that used for evaporation. The film was annealed at a T_{sub} of 550 °C while the powder, T_{src}, was set slightly lower at 545 °C to avoid source condensation on the film. Helium was used as the ambient gas to increase the isothermal nature of the anneal. The proximity anneal using $CdSe_{0.4}Te_{0.6}$ powders was originally developed to maximize 2PE-TRPL decay lifetimes in alumina/Cd(Se,Te)/alumina double heterostructures [40]. When annealing films with higher Se compositions, only slight increases in grain size were observed. However, when annealing $CdSe_{0.10}Te_{0.9}$ films specifically, we observed extremely large and rapid grain growth which we term CGG. For this paper, we will focus on CGG observed in $CdSe_{0.10}Te_{0.9}$ films proximity annealed with $CdSe_{0.4}Te_{0.6}$ powders.

CSS was also used as a deposition technique to deposit CdTe on the CGG templates described above. Unlike annealing, for deposition purposes, the CSS source temperature was maintained higher than the substrate temperature to keep ΔG_v (e.g. equation (2)) negative. In this case, T_{src} establishes the overpressure (P_s) while T_{sub} sets the condensed solid equilibrium pressure (P_o). For our epitaxial study, we varied T_{src} and T_{sub} systematically to vary P_s and P_o respectively, and thus ΔG^* and r^*. The necessary range in $\Delta T = T_{src} - T_{sub}$ required to do this effectively required the use of two different CSS heating strategies. For smaller ΔT, we controlled the source and substrate temperatures independently. In this approach, T_{sub} was fixed at 625 °C while T_{src} was adjusted to 635 °C ($\Delta T = 10$ °C) or 660 °C ($\Delta T = 35$ °C). For larger ΔT (and thus greater P_s/P_o), only the source was heated with the substrate heated indirectly by thermal coupling to the source. Using this second approach, we recorded a substrate temperature of 513 °C at a source temperature of 674 °C ($\Delta T = 161$ °C). To calculate P_s and P_o we used the vapor pressure data of Goldfinger and Jeunehommme, which most accurately represented the temperature range used [41]. The CdTe partial pressure relation was:

$$\log P(\mathrm{CdTe, atm}) = 6.572 - \left({}^{9764}/_{T(K)}\right) \tag{5}$$

Table 1. Relative nucleation parameters for epitaxial CdTe deposition.

T_{src} (°C)	T_{sub} (°C)	ΔT(°C)	P_{src} (atm)	P_{sub} (atm)	$r^* \propto \left(\ln\left(P_{src}/P_{sub}\right)\right)^{-1}$	$\Delta G^* \propto \left(\ln\left(P_{src}/P_{sub}\right)\right)^{-2}$
674	513	161	1.83×10^{-4}	1.41×10^{-6}	0.206	0.042
660	625	35	1.28×10^{-4}	5.00×10^{-5}	1.065	1.134
635	625	10	6.59×10^{-5}	5.00×10^{-5}	3.627	13.153

We then calculated the relative magnitude of ΔG_v, and thus, and ΔG^* using equations (2), (3*b*), and (4) with the assumption of similar contact angles since growth surfaces and condensed phases were similar. Table 1 shows the resulting relative estimates of these nucleation parameters for the experimental growth conditions subsequently discussed in the Results and Discussion section. ΔG^* and r^* are of arbitrary energy and length units, respectively.

2.2. Characterization

Electron back scatter diffraction (EBSD) analysis was performed in a Thermo Fisher Nova NanoSEM 630 field-emission scanning electron microscope (SEM) to quantify crystalline grain size and orientation. Part of the EBSD data was taken using an EDAX Pegasus/Hikari A40 system using a CCD camera and part with an Oxford AZtecHKL system with Symmetry EBSD detector using a CMOS sensor. To avoid shadowing effects and to prepare high-quality cross sections for the EBSD analysis, the samples were prepared using the following procedure: encapsulation using a small piece of high-conductivity Si wafer and Ag-conductive epoxy; mechanical polishing in an Allied High Tech MultiPrep system, using 30, 9, and 3 μm m grid diamond lapping films; and ion milling in a JEOL cross-section polisher.

For general imaging of grains, bright-field optical microscopy images were obtained using a Zeiss M2m Imager with AxioVision software at 500X magnification. A Wyko optical profilometer (Veeco) measured the average (R_a), root-mean square (R_q), average of difference between five highest peaks and five lowest valleys (R_z), and maximum distance between highest and lowest vertical points (R_t) values over different scan areas. 2.5 ×, 20 ×, and 50 × objectives examined regions of 1.9 × 2.4 mm (3.3 μm lateral resolution), 227 × 299 μm (407 nm lateral resolution), and 91 × 120 μm (163 nm lateral resolution), respectively.

XRD was performed with a Rigaku DMAX Diffractometer using CuKα radiation from a rotating anode at 40 kV and 250 mA excitation. Typical scans were performed from 20° to 90° 2θ. Slits were used to keep the incident beam size smaller than the sample at all scanned angles. Any variations in incident beam intensity was eliminated by normalizing collected data with a NIST XRD Flat-Plate Intensity Standard (SRM 1976) so that absolute intensity could be quantitatively compared.

3. Results and discussion

3.1. Colossal grain growth (CGG)

Evaporated $CdSe_{0.1}Te_{0.9}$ films on polycrystalline alumina and (Mg,Zn)O had very small grain sizes (∼100's nm) typical of the growth conditions described previously. After the CSS-proximity anneal using a $CdSe_{0.4}Te_{0.6}$ anneal powder, CGG up to mm-grain sizes were reproducibly observed. The typical morphology before and after CGG for an evaporated $CdSe_{0.1}Te_{0.9}$ film on alumina is shown in figure 2.

The columnar, fiber-like structure of the as-deposited film seen in figure 2(a) at 0° tilt exhibits a uniform grain size on the order of 200 nm with the slight textured growth a result of the film being slightly non-normal to the evaporant source. Figure 2(b) is a similar SEM view at 0° tilt of the same film after the CGG process but at a greatly reduced magnification of only 304X. The grains shown here are on the order of ⩾500 μm representing a 3-order magnitude grain growth due to CGG. The GBs of individual grains are clearly seen. Also visible at this scale within grains are twin domains which appear to be slightly curved, perhaps resulting from how the grains were formed. The single crystal nature of these large grains is shown in the EBSD image of figure 2(c). In this and subsequent EBSD images, the color of a GB was arbitrarily set as 'white' while twin boundaries were assigned as 'black'. All EBSD images are inverse-pole figures (IPFs) where the orientation of grains in the image normal to the substrate can be determined by using the accompanying 'color triangle'. The absence of any 'white' lines in figure 2(c) is proof of the single-crystal nature of the large grains shown in figure 2(b). At the same time, the black, parallel lines represent twin boundaries separating two different domains which for this sample, correspond to regions of the crystal where the (223) and (233) plane normals are perpendicular to the substrate. The <111> growth direction in this example is not exactly perpendicular to the substrate though it is close (i.e. interplanar angles for the two domains relative to the (111) plane are 10.0° and 11.4° respectively). Figure 2(d) shows higher detail of a twinned region that

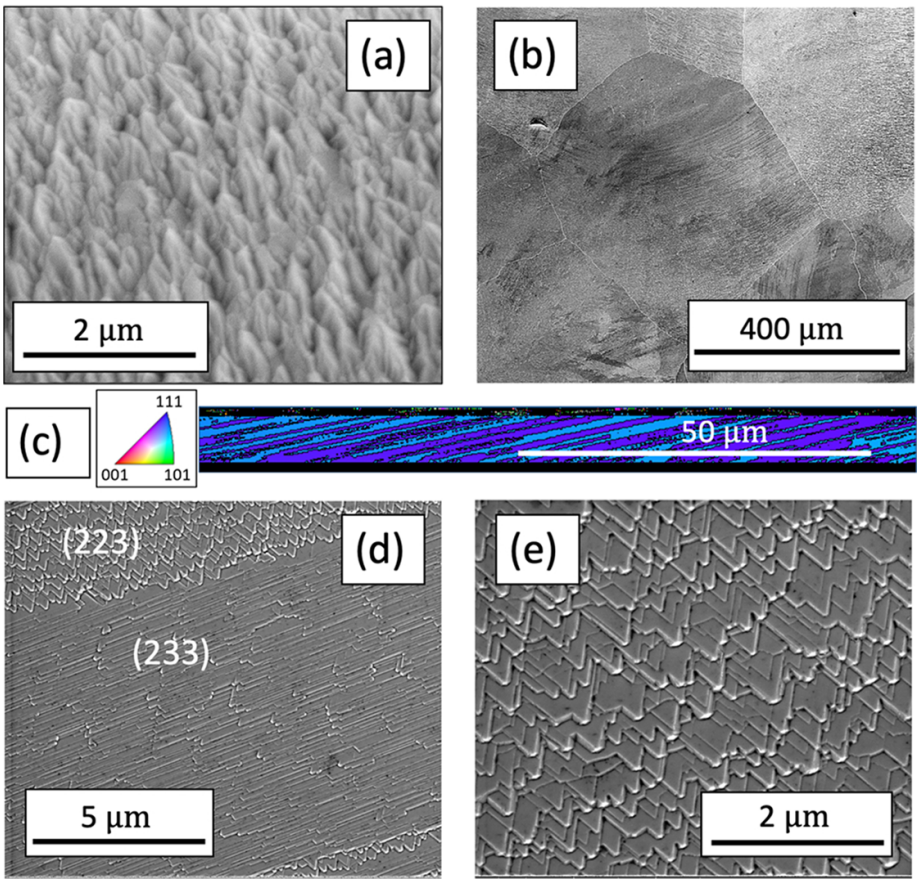

Figure 2. SEM images of $CdSe_{0.1}Te_{0.9}$ thin film *before* (a), and *after* CGG ((b), (d), and (e)), with EBSD inverse-pole-figure (showing grain orientation perpendicular to the substrate) cross-section and orientation color triangle (c) for a single grain. Initial SEM magnification for (a), (b), (d), and (e) were 20 kX, 304 X, 20 kX, and 50 kX respectively. All SEM images taken at 0° tilt. EBSD image obtained at 4.7 kX and tilt of 30°.

intersects the surface of the film where triangular and rectangular habits were indexed by EBSD as the (223) and (233) planes, respectively. Finally, figure 2(e) was taken at the same magnification as figure 2(a) and shows the terraced habit of the (223) domain on the film surface.

Grains measuring up to 1 mm correspond to a GS/t ratio of ∼167 which is significantly greater than what has been commonly seen when using $CdCl_2$ anneals. The grain growth shown in figure 2 is distinctly different from the classic film nucleation and growth physics presented in the introduction.

XRD was performed on the starting evaporant source powder as well as the film before and after the CGG process. To quantify changes induced by the CGG process, an alumina intensity calibration plate (SRM 1976) was measured before each of the latter two measurements to normalize beam intensity. Diffraction data using both a log intensity scale of the (111) diffraction peak and linear scale for all peaks is shown in figures 3(a) and (b).

In figure 3(b), the diffraction pattern for the $CdSe_{0.1}Te_{0.9}$ source powder is also included. The cubic lattice parameter, a_o, for the starting powder and evaporated film before and after CGG was determined by extrapolating $\cos^2\theta/\sin\theta$ to zero to minimize measurement error [42]. The respective lattice parameters were 6.449, 6.458, and 6.450 Å. As reported by Strauss [43], the lattice parameter decreases with increasing Se. The value of 6.449 Å we measured for the powder sample agrees well with the value reported by Strauss for the 10% alloy (6.444 Å). Though overall changes in at.% Se for the observed variation in lattice constant are small (approximately 0.02 at.%), the increase in a_o during condensation suggests a slight loss of Se. At the same time, the subsequent Se-anneal during the CGG process appears to re-introduce Se to match the starting composition of the powder.

The most significant observation from the XRD data is the diffracted intensity before and after CGG. For instance, the corresponding normalized peak intensity for the (111) peak before and after CGG were 2.8×10^4 and 1×10^6 cps, respectively, indicating a significant increase in (111) orientation. The increase in this orientation is also demonstrated by the appearance of the (222) peak which is seen in the diffraction of single crystals, but not typically polycrystalline samples. Though not quantified, the integrated intensity is

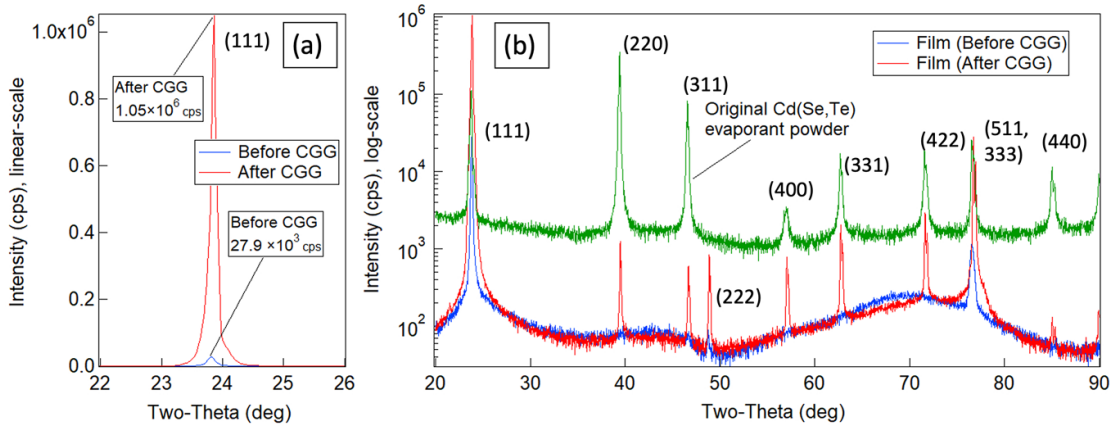

Figure 3. Intensity calibrated x-ray diffraction patterns for Cd(Se,Te) alloy films before and after the CGG process. Scans performed at 1° min^{-1} in continuous mode with data obtained at 0.02° increments.

also significantly higher suggesting significantly improved crystallinity. Normal evaporated and CSS thin films of CdTe and Cd(Se,Te) consist of smaller grains, often with very small concentrations of secondary as well as amorphous phases, which can reduce overall integrated peak intensities. The two-order magnitude increase in XRD intensity after CGG growth corroborates the large-grain, near single-crystal nature of these CGG films.

We believe the CGG process is most similar to 'explosive' crystallization first reported by Gore in 1855 as resulting from the amorphous-to-crystalline phase transformation seen in electrolytically deposited Sb films [44]. This phenomena was extensively researched in the 1970s and 1980s for amorphous Si and Ge films with several reviews written [45, 46]. These studies described 'explosive' crystallization as the lateral propagation of crystallizing molten growth fronts at linear velocities on the order of cm s^{-1} to m s^{-1}. However, the final grain size was not nearly as large as that shown in figure 2(b). Instead, grain size was typically limited to tens of microns, with only a few cases where grain sizes up to hundreds of microns were reported. Large lateral grain growth involved three different stages: (a) initiation, (b) propagation, and (c) quenching (termination). Initiation was always a necessary step and consisted of perturbing films by laser pulses [47–51], mechanical impact [52, 53], furnace heating [54–56], or electron beams [57, 58]. In most studies, growth was considered to be initiated and propagated by the continuous release of latent crystallization heat and melting to explain the spontaneous kinetics of high velocity growth fronts. In the case of sputtered Cu films [55], the latent energy was based on strain due to metastable orientation. Termination was a less understood topic, though mechanisms included the drag effect of impurities as well as the gradual loss of energy associated with heat dissipation through radiation or convection [45, 46].

Several aspects of 'explosive' crystallization are relevant to the CGG process. First, the rate of grain growth appears to be quite high. The thermal mass of the CSS equipment prevented us from determining accurate growth velocities since large, finite times are required to both heat and cool samples. However, we have observed CGG effects in $CdSe_{0.1}Te_{0.9}$ films simply heated to 550 °C at which point heating is turned off, i.e. no intentional temperature soak. If we assume, an anneal time of 1 s, the corresponding growth velocity is approximately 1000 μ s^{-1} or 0.1 cm s^{-1}. In comparison, 20 μm grains resulting from traditional $CdCl_2$ anneals in 10 min would correspond to a growth velocity 0.03 μm s^{-1}, which is five orders of magnitude slower.

Solid-state diffusion cannot explain the observed incredible growth rates at a process temperature of 550 °C. The Cd and Te self-diffusion are on the order of $\sim 10^{11}$ cm^2 s^{-1} at this temperature, corresponding to a diffusion length of $\sim$1 μm. This is more likely to explain the secondary crystallization effects shown in figure 1(c) when $CdCl_2$ is present but not what is happening in CGG.

Like 'explosive' crystallization, melting likely facilitates such rapid mass transfer. However, the mechanism for melting and propagation is unclear for CGG. In 'explosive crystallization', the latent heat released during crystallization to support propagation seems reasonable. Assuming a 1 μm thick a-Si film, a reported s-Si density of 2.28 gm cm^{-3} [59], a specific heat near that of Si (=0.7 J $gm^{-1} \cdot$ °C), and a latent heat of 11.9 kJ $mole^{-1}$ [60], the resulting temperature rise per cm^2 film is close to the melting temperature. However, no such latent heat is readily available in the case of CGG in our $CdSe_{0.1}Te_{0.9}$ alloys. As shown in figure 3, condensed films appear to be polycrystalline and not amorphous. It is also not simple to explain the effect as resulting from the very low surface energy of elemental Se at its melting temperature of 220 °C [61]

Figure 4. Initial nucleation (a) and final film surface (b) for CdTe growth on CGG Cd(Se,Te) templates. Images provided by optical microscopy at a magnification of 500X.

since again, CGG does not appear to occur in films with higher Se concentrations than $CdSe_{0.1}Te_{0.9}$. The fact that CGG only occurs in $CdSe_xTe_{1-x}$ films when $x \sim 0.1$ is perplexing.

The substrate surface roughness upon which the Cd(Se,Te) alloy is evaporated appears to have a significant role on whether CGG occurs. CGG occurs strongly when the surface roughness, as measured by the Wyco optical profilometer, is less than ~1.0–1.5 nm, and is greatly attenuated when the roughness exceeds 2.0 nm. This could be problematic when considering conventional SnO_2-coated substrates used for solar cell applications where the roughness is typically greater than 10 nm. The limiting role of surface roughness points to the importance of surface chemistry or wetting that occurs between the film and oxide-coated substrate. Topography (i.e. roughness), is well known to affect wetting [62, 63]. In general, increased roughness has the effect of decreasing the wetting nature of substrates and this can help explain observed correlations between CGG and surface roughness.

3.2. CGG film templates for CdTe epitaxy

CGG $CdSe_{0.1}Te_{0.9}$ films on alumina-coated glass substrates were used as large-grain templates for attempting CdTe epitaxy. Though CdTe films could be readily deposited on these templates, the deposited CdTe morphology was extremely rough and facetted. Subsequently, we used much shorter CdTe deposition times to better understand film nucleation. Figure 4(a) shows an optical microscope image of the initial film growth nucleation while figure 4(b) shows the resulting final film morphology.

In figure 4(a), GBs between individual large $CdSe_{0.1}Te_{0.9}$ grains were decorated with nucleating CdTe crystallites. Some nucleation also occurred on grains away from GBs but with much lower density and slower growth rates (larger grains located on GBs). The convolution of different grain sizes, nucleating sites, and growth rates was problematic for epitaxy and resulted in very faceted and disordered alignment of CdTe crystallites resulting in surface roughness on the order of the film thickness as seen in figure 4(b), which is not suitable for thin film PV devices. The different growth rates between and at GBs is likely due to higher adatom residence at GB imperfections relative to the smoother, intragranular regions.

To circumvent this undesired bimodal growth behavior, a small amount of oxygen was introduced into the CSS chambers during the CdTe deposition. Oxygen is well known to behave as a nucleating agent in CSS deposited CdTe [64]. All depositions subsequently discussed involved a growth ambient consisting of 0.75 Torr oxygen with 14.25 Torr Helium. With oxygen, our intent was to increase adatom residence time in the smoother region between GBs so that growth would occur more uniformly. In a previous CdTe epitaxy study using large-grain templates [38], we used single-crystal MBE and smaller-grain (~20 micron) templates and observed epitaxy in both cases using inert or reducing (H_2) ambient. Oxygen was not necessary in this earlier work since either GBs were absent (MBE templates) or the GB density was considerably higher (20 μm grains) such that bi-modal growth patterns did not visibly affect morphology.

By introducing oxygen, we achieved very good epitaxy using the CGG $CdSe_{0.1}Te_{0.9}$ templates. After averaging the growth rate, much smoother films were obtained. In addition, the resulting epitaxial growth appears to follow the conventional nucleation and growth model presented earlier in the introduction. Optical images of the CGG template surface morphology (top-row), resulting optical images of the CdTe surface morphology (middle-row), and cross-sectional EBSD IPF data (bottom-row) for the CSS growth parameters given in table 1 are shown in figure 5. The horizontal-dashed yellow lines shown in the bottom row indicate the starting thickness of the CGG template as measured before CdTe deposition. Morphology

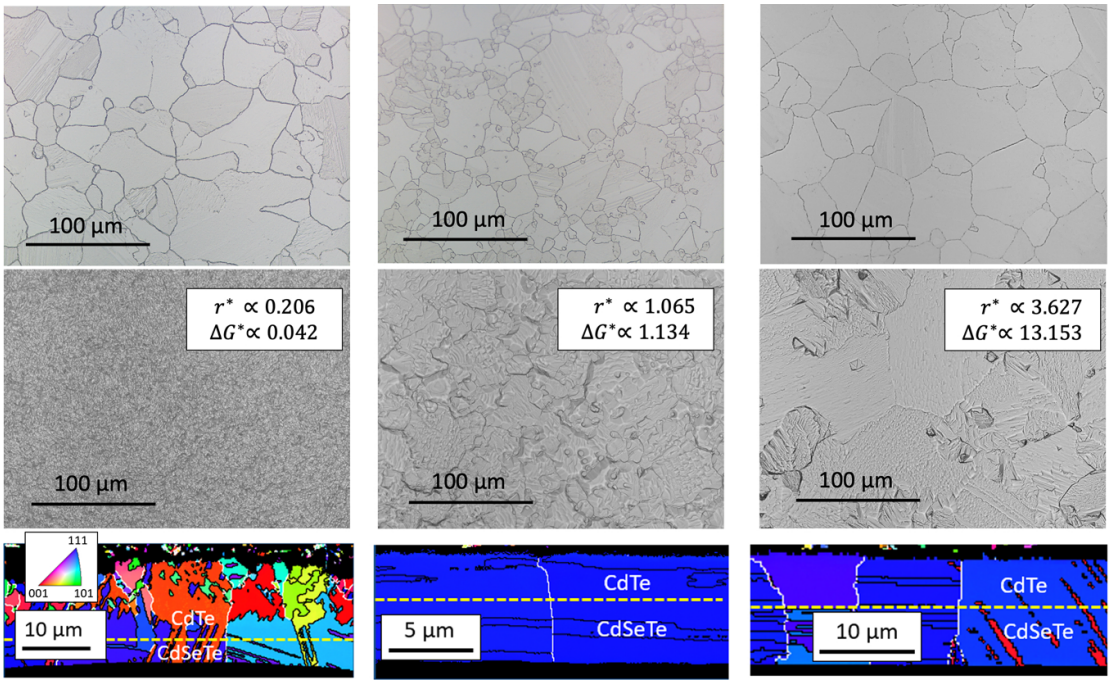

Figure 5. Top Row: optical images (500X) of CdSeTe film template surface; Middle Row: similar optical image after the CdTe deposition by CSS; Bottom Row: inverse-Pole figure EBSD images of grain orientation perpendicular to the substrate (orientation color triangle corresponds to all EBSD images). Left to right columns correspond to different CSS nucleation conditions given by relative changes in r^* and ΔG^* indicated.

above this line shows the quality of the CdTe epitaxy. The CdTe deposition rate was measured at 5.82, 1.15, and 1.36 μm min^{-1} for the columns proceeding left to right respectively. Each column corresponds to different values of r^* and ΔG^* as indicated in the figure. The EBSD color in the IPF map represents the orientation normal to the film surface for both the deposited CdTe film as well as the $CdSe_{0.1}Te_{0.9}$ template.

When growth conditions corresponding to lower r^* and ΔG^* values were used (far-left column of figure 5), the very small stable nuclei radius and energy barrier for growth results in numerous nucleating sites within each individual grain of the $CdSe_{0.1}Te_{0.9}$ template. The resulting morphology consists of many grains on each individual template grain. No preferential growth orientation was observed in this case. However, with increasing r^* and ΔG^*, larger stable nuclei and greater growth barriers reduce the nucleation site density within a template grain leading to strong epitaxy, i.e. a single CdTe grain per individual $CdSe_{0.1}Te_{0.9}$ grain. This is shown in the middle-column. The resulting CdTe surface morphology exhibits a crystal size similar to the crystal size of the template. The single shade of blue also indicates a very strong (111) orientation that matches well with the (111) orientation of the template. The red lines appear to be twins that have occurred during the (111) growth based on their appearance. Interestingly, at the lowest value of $P_s/P_o \sim T_{sub}/T_{src}$ (far-right column), we begin to observe a breakdown in crystal quality—not so much in the deposited CdTe but more interestingly, in the growth template itself. This may indicate that higher substrate growth temperatures (625 °C; middle and far-right columns) require a minimum overpressure, P_s (e.g. T_{src} 635 °C) to stabilize the CGG template during growth. Epitaxy is however still maintained with the grain size of the template replicated in the grain size of the CdTe layer. Finally, note that the same disruption of the growth template observed in the far-right column is also present in the far-left column. We speculate that the template disruption seen at the lower $T_{sub} = 513$ °C is rather due to stress imparted on the template by the strain resulting from the nucleation of many, non-oriented, smaller CdTe grains.

The results shown here provide new paths for CdTe solar cells. The $CdCl_2$ treatment often induces carrier compensation, which can limit V_{oc} either through reduced hole density or the introduction of potential fluctuations resulting from poor dopant activation when achieving hole densities exceeding 10^{16} cm^{-3}. With CGG, $CdCl_2$ is not required for grain growth. The $CdCl_2$ treatment also reduces the ability to utilize the full range of II–VI alloys. For example, CdZnTe and CdMgTe compositions can realize a wide bandgap range. They are easier to dope than CdTe; they can form back surface passivation, reflectors, or fields to increase performance; and they can achieve bandgaps ideally suited for different tandem solar cell applications. However, the $CdCl_2$ treatment causes Mg or Zn to migrate out of the semiconductors, making these alloys ineffective for current state-of-the-art technology. With CGG, extremely large-grained films without $CdCl_2$

are possible and when used as epitaxial template layers, can provide a rapid and inexpensive way to fabricate large grained CdTe and II–VI alloy films and devices.

4. Summary

Polycrystalline $CdSe_xTe_{1-x}$ films with grain sizes orders of magnitude greater than what has previously been reported have been discussed. These films have a grain size-to-film thickness ratio that exceeds 100, exhibit highly oriented (111) growth, and can be used as growth templates for the subsequent epitaxy of CdTe using high-throughput deposition techniques like CSS. CGG is only seen in low selenium-content ($x \sim 0.1$) films, is similar to 'explosive' crystallization and occurs with uniform linear growth velocities on the order of 0.1 cm s^{-1}. Details of the growth process remain unknown, particularly, the mechanisms by which growth initiates and propagates. Of academic interest is the close alignment of subsequent CdTe epitaxy on these templates with conventional nucleation and growth theories. The CGG process provides an inexpensive way to form templates that can be used to epitaxially grow CdTe films that greatly reduce GB recombination and may represent a viable way to reduce or even eliminate the need for $CdCl_2$ as a passivating additive. This may alleviate difficulties in achieving higher GrV dopant activation due to compensation in CdTe solar cells.

Acknowledgments

The material was based on work supported by the U.S. Department of Energy's Office of Energy Efficiency and Renewable Energy (EERE) under Solar Energy Technologies Office (SETO) Contract No. DE-EE0008552, agreements 34345 and 34353. This work was authored in part by the National Renewable Energy Laboratory, operated by Alliance for Sustainable Energy, LLC, for the U.S. Department of Energy (DOE) under Contract No. DE-AC36-08GO28308. The views expressed in the article do not necessarily represent the views of the DOE or the U.S. Government.

Conflict of interest

The authors declare no conflict of interest.

ORCID iD

David S Albin https://orcid.org/0000-0001-9273-5538

References

[1] LAZARD, Ltd 2018 Lazard's levelized cost of energy analysis—version 12.0 (available at: www.lazard.com/media/450784/lazards-levelized-cost-of-energy-version-120-vfinal.pdf)
[2] Moseley J, Grover S, Lu D, Xiong G, Guthrey H L, Al-Jassim M M and Metzger W K 2020 Impact of dopant-induced optoelectronic tails on open-circuit voltage in arsenic-doped Cd(Se)Te solar cells *J. Appl. Phys.* **128** 103105
[3] Metzger W K, Albin D, Romero M J, Dippo P and Young M 2006 $CdCl_2$ treatment, S diffusion, and recombination in polycrystalline CdTe *J. Appl. Phys.* **99** 103703
[4] Major J D, Al Turkestani M, Bowen L, Brossard M, Li C, Lagoudakis P, Pennycook S J, Phillips L J, Treharne R E and Durose K 2016 In-depth analysis of chloride treatments for thin-film CdTe solar cells *Nat. Commun.* **7** 13231
[5] Kephart J M, McCamy J W, Ma Z, Ganjoo A, Alamgir F M and Sampath W S 2016 Band alignment of front contact layers for high-efficiency CdTe solar cells *Sol. Energy Mater. Sol. Cells* **157** 266–75
[6] Ablekim T *et al* 2018 Interface engineering for 25% CdTe solar cells *ACS Appl. Energy Mater.* **1** 5135–9
[7] Bittau F, Potamialis C, Togay M, Abbas A, Isherwood P J M, Bowers J W and Walls J M 2018 Analysis and optimization of the glass/TCO/MZO stack for thin film CdTe solar cells *Sol. Energy Mater. Sol. Cells* **187** 15–22
[8] Ablekim T *et al* 2019 Tailoring MgZnO/CdSeTe interfaces for photovoltaics *IEEE J. Photovolt.* **9** 888–92
[9] Amarasinghe M *et al* 2018 Obtaining large columnar CdTe grains and long lifetime on nanocrystalline CdSe, MgZnO, or CdS layers *Adv. Energy Mater.* **8** 1702666
[10] Paudel N R, Poplawsky J D, Moore K L and Yan Y 2015 Current enhancement of CdTe-based solar cells *IEEE J. Photovolt.* **5** 1492–6
[11] Swanson D E, Sites J R and Sampath W S 2017 Co-sublimation of $CdSe_xTe_{1-x}$ layers for CdTe solar cells *Sol. Energy Mater. Sol. Cells* **159** 389–94
[12] Zheng X *et al* 2019 Recombination and bandgap engineering in CdSeTe/CdTe solar cells *APL Mater.* **7** 071112
[13] Zheng X, Colegrove E, Duenow J N, Moseley J and Metzger W K 2020 Roles of bandgrading, lifetime, band alignment, and carrier concentration in high-efficiency CdSeTe solar cells *J. Appl. Phys.* **128** 053102
[14] Lingg M, Spescha A, Haass S G, Carron R, Buecheler S and Tiwari A N 2018 Structural and electronic properties of $CdTe_{1-x}Se_x$ films and their application in solar cells *Sci. Technol. Adv. Mater.* **19** 683–92
[15] Munshi A H, Kephart J M, Abbas A, Danielson A, Gélinas G, Beaudry J-N, Barth K L, Walls J M and Sampath W S 2018 Effect of $CdCl_2$ passivation treatment on microstructure and performance of CdSeTe/CdTe thin-film photovoltaic devices *Sol. Energy Mater. Sol. Cells* **186** 259–65
[16] Guo J *et al* 2019 Effect of selenium and chlorine co-passivation in polycrystalline CdSeTe devices *Appl. Phys. Lett.* **115** 153901

[17] Metzger W K et al 2019 Exceeding 20% efficiency with *in situ* group V doping in polycrystalline CdTe solar cells *Nat. Energy* **4** 837–45
[18] Duenow J N et al 2016 Relationship of open-circuit voltage to CdTe hole concentration and lifetime *IEEE J. Photovolt.* **6** 1641–4
[19] Krasikov D and Sankin I 2017 Defect interactions and the role of complexes in the CdTe solar cell absorber *J. Mater. Chem.* A **5** 3503–13
[20] Sankin I and Krasikov D 2019 Kinetic simulations of Cu doping in chlorinated CdSeTe PV absorbers *Phys. Status Solidi* a **216** 1800887
[21] McCandless B et al 2018 Overcoming carrier concentration limits in polycrystalline CdTe thin films with *in situ* doping *Sci. Rep.* **8** 14519
[22] Colegrove E, Yang J-H, Harvey S P, Young M R, Burst J M, Duenow J N, Albin D S, Wei S-H and Metzger W K 2018 Experimental and theoretical comparison of Sb, As, and P diffusion mechanisms and doping in CdTe *J. Phys. D: Appl. Phys.* **51** 075102
[23] Burst J M, Farrell S B, Albin D S, Colegrove E, Reese M O, Duenow J N, Kuciauskas D and Metzger W K 2016 Carrier density and lifetime for different dopants in single-crystal and polycrystalline CdTe *APL Mater.* **4** 116102
[24] Burst J M et al 2016 CdTe solar cells with open-circuit voltage breaking the 1 V barrier *Nat. Energy* **1** 1–7
[25] Nagaoka A, Kuciauskas D, McCoy J and Scarpulla M A 2018 High p-type doping, mobility, and photocarrier lifetime in arsenic-doped CdTe single crystals *Appl. Phys. Lett.* **112** 192101
[26] Jensen S A, Glynn S, Kanevce A, Dippo P, Li J V, Levi D H and Kuciauskas D 2016 Beneficial effect of post-deposition treatment in high-efficiency Cu(In,Ga)Se_2 solar cells through reduced potential fluctuations *J. Appl. Phys.* **120** 063106
[27] Kanevce A, Reese M O, Barnes T M, Jensen S A and Metzger W K 2017 The roles of carrier concentration and interface, bulk, and grain-boundary recombination for 25% efficient CdTe solar cells *J. Appl. Phys.* **121** 214506
[28] Romeo A, Khrypunov G, Galassini S, Zogg H and Tiwari A N 2007 Bifacial configurations for CdTe solar cells *Sol. Energy Mater. Sol. Cells* **91** 1388–91
[29] Marsillac S, Parikh V Y and Compaan A D 2007 Ultra-thin bifacial CdTe solar cell *Sol. Energy Mater. Sol. Cells* **91** 1398–402
[30] Nardone M, Spehar M, Kuciauskas D and Albin D S 2020 Numerical simulation of high-efficiency, scalable, all-back-contact Cd(Se,Te) solar cells *J. Appl. Phys.* **127** 223104
[31] Thomson C V and Carel R 1995 Texture development in polycrystalline thin films *Mater. Sci. Eng.* B **32** 211–9
[32] Kenty J L and Hirth J P 1969 Epitaxy and heterogeneous nucleation theory *Surf. Sci.* **15** 403–24
[33] Winger J R and Scarpulla M A 2019 Grain growth in CdTe films during $CdCl_2$ Treatment: $TeCl_4$ theory *IEEE 46th Photovoltaics Specialists Conf.* pp 1823–38
[34] Enriquez J P and Mathew X 2005 Anneal induced recrystallization of CdTe films electrodeposited on stainless steel foil: the effect of $CdCl_2$ *J. Mater. Sci., Mater. Electron.* **16** 617–21
[35] Atapattu H Y R, De Silva D S M and Pathiratne K A S 2018 Post deposition surface treatments to enhance the quality of polycrystalline CdTe thin films for photovoltaic applications *Mater. Chem. Phys.* **213** 406–13
[36] Jensen S A 2016 Long carrier lifetimes in large-grain polycrystalline CdTe without $CdCl_2$ *Appl. Phys. Lett.* **108** 263903
[37] Albin D S et al 2019 U.S. Patent No. 10, 304,989 (Washington, DC: U.S. Patent and Trademark Office)
[38] Colegrove E, Albin D S, Moutinho H R, Amarasinghe M, Burst J M and Metzger W K 2020 Scalable ultrafast epitaxy of large-grain and single-crystal II–VI semiconductors *Sci. Rep.* **10** 2426
[39] *5N Plus, 4385 Garand Street, Montreal, Quebec Canada*
[40] Kuciauskas D et al 2019 Radiative efficiency and charge-carrier lifetimes and diffusion length in polycrystalline CdSeTe heterostructures *Phys. Status Solid* **14** 1900606
[41] Goldfinger P and Jeunehomme N 1963 *Trans. Faraday Soc.* **59** 2851
[42] Cullity B D 1978 *Elements of X-ray Diffraction* 2nd edn (Reading, MA: Addison-Wesley) pp 359–60
[43] Strauss A J and Steininger J 1970 Phase diagram of the CdTe-CdSe pseudobinary system *J. Electrochem. Soc.* **117** 1420–6
[44] Gore G 1855 *Phil. Mag.* **9** 73
[45] Bensahel D and Auvert G 1983 Explosive crystallization in a-Ge and a-Si: a review *Mat. Res. Soc. Symp. Proc.* **13** 165–76
[46] Aleksandrov L N and Edelman F L 1983 Shock crystallization of films *Phys. Status Solidi* a **76** 409–27
[47] Chapman R L, Fan J C C, Zeiger H J and Gale R P 1980 Crystallization-front velocity during scanned laser crystallization of amorphous Ge films *Appl. Phys. Lett.* **37** 292–5
[48] Leamy H J, Brown W L, Celler G K, Foti G, Gilmer G H and Fan J C C 1981 Explosive crystallization of amorphous germanium *Appl. Phys. Lett.* **38** 137–9
[49] Thompson M O, Galvin G J, Mayer J W, Peercy P S, Poate J M, Jacobson D C, Cullis A G and Chew N G 1984 Melting temperature and explosive crystalllization of amorphous silicon during pulsed laser irradiation *Phys. Rev. Lett.* **52** 2360–3
[50] Narayan J, Pennycook S J, Fathy D and Holland O W 1984 Explosive recrystallization during pulsed laser irradiation *J. Vac. Sci. Technol.* A **2** 1495–7
[51] Cullis A G 1985 Fundamental aspects of high speed crystal growth from the melt *Mat. Res. Soc. Symp.* **35** 15–24
[52] Takamori T, Messier R and Roy R 1972 New noncrystalline germanium which crystallizes 'Explosively' at room temperature *Appl. Phys. Lett.* **20** 201–3
[53] Mineo A, Matsuda A, Kurosu T and Kikuchi M 1973 Observations of propagation in shock-crystallization of sputtered amorphous germanium films *Solid State Commun.* **13** 1307–10
[54] Messier R, Takamori T and Roy R 1975 Observations on the 'Explosive' crystallization of non-crystalline Ge *Solid State Commun.* **16** 311–4
[55] Takewaki T 1995 Formation of giant-grain copper interconnects by a low-energy ion bombardment process for high-speed ULSIs *Mat. Chem. Phys.* **41** 182–91
[56] Pore V, Ritala M, Leskelä M, Saukkonen T and Järn M 2009 Explosive crystallization in atomic layer deposited mixed titanium oxides *Cryst. Growth Des.* **9** 2974–8
[57] Das V D and Lakshmi P J 1988 Electron-beam-induced 'explosive' crystallization of amorphous $Se_{80}Te_{20}$ alloy thin films and oriented growth of crystallites *Phys. Rev.* B **37** 720–6
[58] Sharma R K, Bansal S K, Nath R, Mehra R M, Bahadur K, Mall R P, Chaudhary K L and Garg C L 1984 Electron beam induced explosive crystallization of unsupported amorphous germanium thin films *J. Appl. Phys.* **55** 387–94
[59] Custer J S, Thompson M O, Jacobson D C, Poate J M, Roorda S, Sinke W C and Spaepen F 1994 Density of amorphous Si *Appl. Phys. Lett.* **64** 437–9
[60] Donovan E P, Spaepen F, Turnbull D, Poate J M and Jacobson D C 1983 Heat of crystallization and melting point of amorphous silicon *Appl. Phys. Lett.* **42** 698–700

[61] Keene B J 1993 Review of data for the surface tension of pure metals *Int. Mater. Rev.* **38** 157–92
[62] Söz C K, Yilgör E and Yilgör I 2015 Influence of the average surface roughness on the formation of superhydrophobic polymer surfaces through spin-coating with hydrophobic fumed silica *Polymer* **62** 118–28
[63] Bormashenko E 2011 General equation describing wetting of rough surfaces *J. Colloid Interface Sci.* **360** 317–9
[64] Rose D H, Hasoon F S, Dhere R G, Albin D S, Ribelin R M, Li X S, Mahathongdy Y, Gessert T A and Sheldon P 1999 Fabrication procedures and process sensitivities for CdS/CdTe Solar Cells *Prog. Photovolt., Res. Appl.* **7** 331–40